# Closed-loop Optogenetic Control in a Microplate Reader

Hari R. Namboothiri[1†], Krishna Pochana[2†], Bhavya Jaiswal[1], Azita Emami[2], Chelsea Y. Hu[1,2 *]

1. Department of Chemical Engineering, Texas A&M University, College Station, TX 77843
2. Division of Engineering and Applied Science, California Institute of Technology, Pasadena, California, 91125

†. These authors contributed equally.
* Correspondence: Chelsea Y. Hu, Department of Chemical Engineering, Texas A&M University, College Station, TX 77843, Email: chelsea.hu@tamu.edu

Key words: LEMOS, optogenetic feedback control, growth-aware gene expression dynamics, cybergenetics

## Abstract

Living cells sense diverse molecules and synthesize complex compounds, but their responses are slow and context dependent, which makes precise control difficult. Electronic systems excel at fast computation, communication, and control, but their direct access to biochemistry is limited. These two classes can be integrated through optogenetics to form cell-silicon systems for sensing and biomanufacturing. However, prototyping these systems remains nontrivial: current tools either pair high-accuracy sensing with robotic sample transfer that requires extensive setup, or avoid transfers by using custom sensors with limited accuracy and dynamic range that compromise performance. Here we present LEMOS, a low-cost LED-embedded microplate that operates inside a commercial microplate reader, keeping cultures in the reader for the entire experiment while synchronizing illumination with measurement. Using LEMOS and a growth-aware multiscale model, we rapidly executed the design–build–test–learn cycle to diagnose and correct closed-loop overshoot in gene-expression setpoint tracking. We demonstrate closed-loop gene-expression control in batch culture within a standard plate reader and show that growth state is a key design variable for controller choice and tuning. By combining accessible hardware with a predictive model, LEMOS lowers the barrier to model-informed DBTL, shortens iteration, and provides a path to portable control strategies that extend to other hosts and optogenetic systems.

## Introduction

Living cells, shaped by evolution, sense a wide diversity of molecules and convert these signals into coordinated gene expression and synthesis of complex organic compounds. Yet cellular responses are slow, noisy, and context dependent, which makes precise regulation difficult. Electronic systems have limited direct access to chemicals but excel at high-speed signal transduction, computation, communication, and control. Combining the two yields cell-silicon hybrids that pair biochemical breadth with engineered precision, enabling remote sensing and adaptive biomanufacturing. Development of such an integrated cell-silicon system has become possible through the establishment of bidirectional communication: light can modulate gene expression through optogenetic control, while fluorescent or luminescent protein reporters can relay gene expression readouts as electronic signals through photodiodes[1-3].

Optogenetics uses light to control cellular processes, enabling rapid, reversible, and precise spatiotemporal regulation of gene expression, capabilities that chemical inducers often lack[4]. Such control has been implemented at the transcriptional[5-9], translational[10,11], and post-translational levels[12-14]. For example, the classic light-responsive CcaSR system comprising a photoreceptor histidine kinase and a response regulator enable reversible activation and repression of transcription[6]. A remaining practical hurdle for cell-silicon control in typical labs is coupling real-time monitoring with dynamic illumination in standard microplate readers. Prior solutions achieve closed-loop regulation using chemostats with robotic sampling[15,16] or single-cell feedback via automated microscopy in a mother-machine[17-19]. However, the complexity and cost of these platforms limit adoption and slows the design-build-test-learn cycle. To overcome these issues, Steel, H. et al.[20] developed a custom miniaturized chemostat that enabled closed-loop optogenetic control, though the device's utility is constrains by the sensor's limited dynamic range. Additionally, these platforms maintain steady-state growth, which eliminate the growth dynamics that arise in batch and other non-constant growth conditions, constraining applicability.

The most common assay in synthetic biology grows cultures in well plates and uses a commercial microplate reader to measure optical density (OD) and fluorescence. External LED-array stimulators have been built to modulate light[21-25], but typically require a human operator[26] or a robotic stage to transfer to a microplate reader[27] for measurement. Several all-in-one platforms combine illumination with onboard fluorescence and $OD_{600}$ sensing for closed-loop control, yet performance is limited by the sensing hardware[28,29]. RT-OGENE uses a digital camera on a stationary stage to read fluorescence and $OD_{600}$, which narrows dynamic range. The system also does not allow shaking, reducing growth and sustained expression[28]. The optoPlateReader moves forward with an LED and photodiode sensor and allows shaking, but it supports only a single reporter and has limited sensitivity for both fluorescence and $OD_{600}$[29]. Both studies attempted feedback control; however, sensor limitations and the lack of an accurate gene expression model constrained controller performance. As a result, progress toward practical cell-silicon hybrid systems has been limited, and there remains a need for an easy-to-use, reader-compatible platform for closed-loop studies in batch culture that accelerates the DBTL cycle.

In this work, we built the LED-Embedded Microplate for Optogenetic Studies (LEMOS) device as a prototyping platform and demonstrated its utility in the DBTL cycle for cell-silicon hybrid dynamical systems. LEMOS is a low-cost (≈$140), LED-embedded microplate that operates inside a commercial microplate reader and synchronizes illumination with measurement by blanking LEDs during reads. In batch *E. coli* cultures, we first mapped open-loop responses, then showed that proportional control tracks predefined setpoints, although with significant overshoot. Using our growth-dependent gene expression framework (GEAGS)[30], we found that the observed dynamics arise from growth-dependent dead time in gene expression and predicted that adding integral and derivative actions would improve performance. Guided by the model, we designed and implemented Proportional-Integral (PI) and Proportional-Integral-Derivative (PID) controllers that improved both accuracy and response speed across conditions. By enabling feedback without leaving the microplate reader, LEMOS makes *in silico* feedback control practical in batch culture, lowers the barrier to rapid DBTL, and is readily extendable to other bacterial strains and optogenetic mechanisms.

## Results

### *LEMOS Device Design and Validation*

The LEMOS device is designed to match the layout of a standard 96 well microplate, ensuring compatibility with conventional microplate readers (Figure 1a). The 3D printed frame houses 16 slots for polydimethylsiloxane (PDMS) microwells, each with an individually addressable light-emitting diode (LED) mounted on the inner wall. The LEDs are controlled by an Arduino Nano33 IoT microcontroller with built in Bluetooth, enabling wireless communication with an external computer. The microcontroller and the LEDs are powered by a Li-ion battery housed within the device, connected to the charging module and a three-position switch that toggles between 'On', 'Off' or 'Charging' modes. The detailed electronic components can be found in Supplementary Information (SI) Section 1 and the operation of the electronic components is described in Methods. To ensure sterility during cell culture experiments, PDMS sleeves are cast for each use via soft lithography (see Methods). PDMS is a transparent, biocompatible elastomer well-suited for microwell fabrication due to its flexibility, chemical inertness, and ease of molding. Its optical transparency also enables fluorescence measurements during experiments. To ensure optimal optical transparency and well-to-well uniformity, air bubbles generated during mixing of the PDMS base and curing agent were carefully removed prior to casting. A 3D-printed mold (Figure 1c) was inserted into the LEMOS frame during casting (Figure 1b) to form wells shaped for incubation of 200 µl bacterial cultures (Figure 1d).

To assess whether LED-generated heat affects cell growth, we monitored bacterial cultures over 16 hours in the LEMOS device using continuous $OD_{600}$ measurements in a standard microplate reader at both 30 °C and 37 °C. As shown in Figures 1e and 1f, cell growth at 37 °C indicating that heat emitted by the LEDs had minimal impact on its growth condition. Cultures at 30 °C exhibited a prolonged exponential phase compared to those at 37 °C (Figures 1e and 1f). Therefore,

all subsequent experiments in LEMOS were conducted at 30 °C to maximize the dynamic measurement window before stationary phase onset.

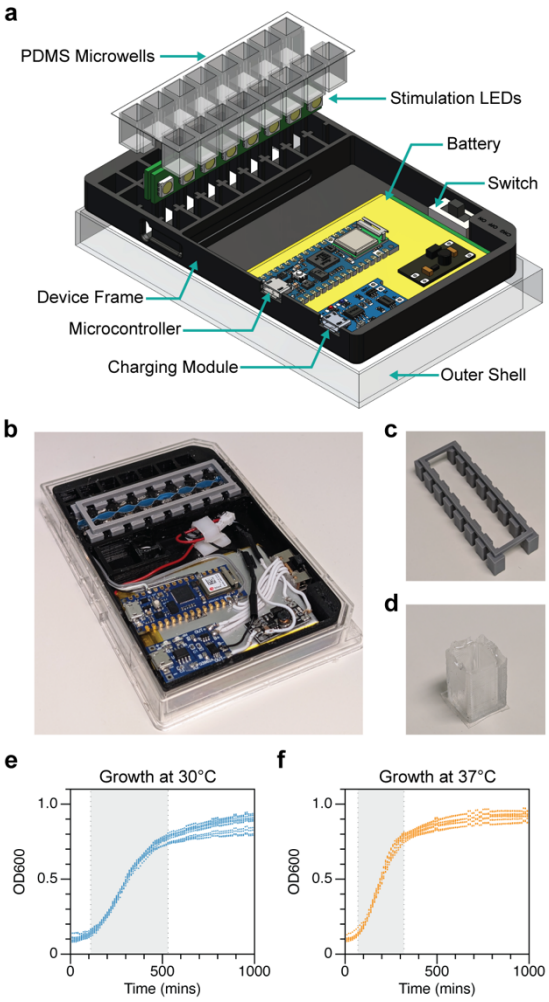


***Figure 1 LEMOS device construction and cell growth characterization.*** *(a)* Exploded schematic of the LEMOS Device showing PDMS microwells, stimulation LEDs, battery, switch, microcontroller, charging module, device frame, and outer shell. (b) Assembled device with the 3D-printed mold used to cast the PDMS microwells. (c) 3D-printed mold for microwell casting. (d) PDMS microwell casted in the LEMOS device (e) Growth curves of *E. coli* in LEMOS at 30 °C and (f) 37 °C (N=12 technical replicates). Gray shading marks the logarithmic (exponential) growth phase.

### *System Characterization and Open-Loop Optogenetic Control*

We used the CcaSR two-component system (TCS) optogenetic regulator system to control expression of superfolder green fluorescent protein (sfGFP). The system consists of CcaS, a membrane-bound histidine kinase that senses green light, and CcaR, the corresponding response regulator[6] (Figure 2a). Upon green light exposure, CcaS autophosphorylates and transfers the phosphate to CcaR, which dimerizes to activate the PcpcG2 promoter and induce sfGFP transcription. Red light reverses this process by promoting CcaS dephosphorylation, thereby repressing expression. To characterize the system, we performed a bulk fluorescence assay in a 96-well microplate. Cultures were incubated at 37 °C under specific light conditions in a custom light box, and fluorescence was measured manually every hour, for six hours, using a microplate reader. The system

functioned as expected in *E. coli* MG1655, with sfGFP activation under green light, repression under red, and intermediate expression in the dark due to basal promoter activity (Figure 2b).

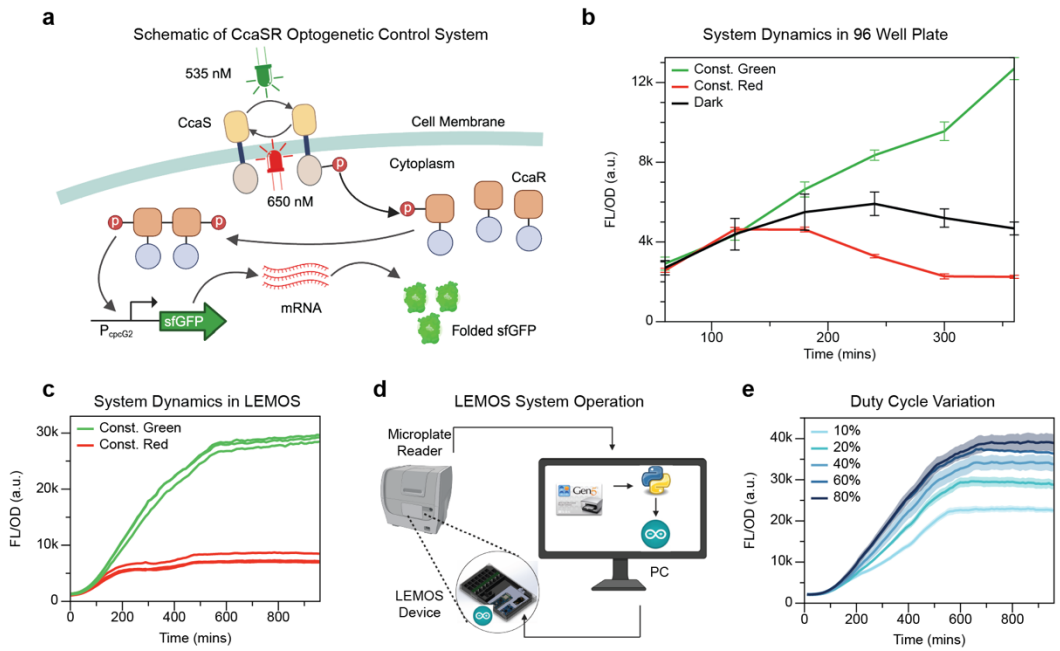


***Figure 2 Optogenetic system characterization in LEMOS and open-loop control dynamics.*** (a) CcaSR two-component optogenetic system: green light (535 nm) activates CcaS/CcaR to upregulate PcpcG2-sfGFP expression, and red light (650 nm) downregulates the expression. (b) Activation-repression dynamics in sfGFP fluorescent/$OD_{600}$ in a standard 96-well plate (n=4) under LED illumination; the plate is manually transferred to the microplate reader for measurement six times over six hours. (c) Same assay in the LEMOS device (N=3) for 16 hours, with one measurement every 10 minutes. (d) LEMOS operation schematic. During the 16-hour time course, the device remains in the microplate reader. The reader measures GFP fluorescence and $OD_{600}$ and streams data to a computer, which handles timekeeping and operates Arduino routines that command the on-board microcontroller to temporarily disable LED illumination during each measurement. (e) Open-loop responses in LEMOS to varying green-light duty cycles (10-80%, N=3). Solid lines indicate means; shaded bands indicate standard deviations. N denotes the number of technical replicates; n denotes for the number of biological replicates.

To enable continuous measurement, we inoculated the same cell lines within the microwells of the LEMOS device and incubated it in a microplate reader. One key requirement for this setup was to prevent interference from the LEMOS LEDs with the optical measurements taken by the microplate reader. To address this, we ensured synchronization between the LEMOS device and an external computer, which handled timekeeping and communicated with the device via Bluetooth. The microplate reader was programmed to record $OD_{600}$ and fluorescence every 10 minutes. During each interval, the LEDs were programmed to turn off during the first and last minute to avoid signal interference during measurements. As shown in Figure 2c, this setup allowed real-time monitoring of sfGFP expression dynamics under both green and red light over a 16-hour time course, with measurements taken every 10 minutes.

To evaluate the system's response actuating parameters, we characterized its dynamics under varying duty cycles. Duty cycle refers to the fraction of time within an interval during which green light is applied, with red light used for the remainder. Our control period is set to be 10

minutes, then the LEDs were on for 8 minutes every interval, during which we varied the proportion of green and red light. A 100% duty cycle corresponds to constant green light, while 0% corresponds to constant red light. As shown in Figure 2e, we tested duty cycles ranging from 10% to 80%. The resulting sfGFP expression levels exhibited a clear positive correlation with duty cycle, indicating sensitive responses of system output (sfGFP signal) to the actuating parameter (duty cycle).

***Closed Loop proportional feedback Control for Setpoint Tracking***

Next, we implemented closed-loop cell-silicon feedback control for setpoint tracking using the LEMOS device. Setpoint tracking is a standard closed-loop task in chemical engineering that drives a measured system variable to a defined value. In this setup, as shown in Figure 2a, gene expression in living bacterial cells serves as the process plant, with sfGFP fluorescence as the output. The microplate reader senses this output and transmits the data to an external computer acting as the controller. Based on the measured signal, the computer calculates control actions and sends commands to the LEMOS microcontroller, which adjusts the LED duty cycle (the actuator) to regulate gene expression via optogenetic input (Figure 3a). In our case, the setpoint is a predefined $FL/OD_{600}$ intensity that signifies the amount of sfGFP expressed per cell on average.

To evaluate setpoint tracking, we assigned two distinct setpoints to two groups of microwells, corresponding to the orange and purple dotted lines in Figure 3b. The controller continuously compared the measured fluorescence to each well's assigned setpoint and computed the LED duty cycle for the next 10-minute control interval. We first implemented Proportional control (P-control), where the duration of green light exposure in each cycle ($t_{green}$) is computed as:

$$t_{green} = K \cdot \big(e(t)\big) \tag{1}$$

Here $e(t)$ is the error between the measured $FL/OD_{600}$ signal and the setpoint at time $t$, and $K$ is the proportional gain that determines the controller's response sensitivity. The remaining portion of the 8-minute control interval not occupied by green light was filled with red light. Because no measurement is available at $t = 0$, the controller initializes with a default 50% duty cycle for the first two intervals. Figure 3c and 3d illustrated how the duty cycles change over time for the two setpoints. In these plots, the height of each green bar represents the fraction of green lights (i.e., the duty cycle) applied during each 8-minute control period. As expected, the duty cycle decreases rapidly as the measured sfGFP approaches the setpoint eventually reaching 0% once signal reaches the setpoint. As shown in Figure 3b, both setpoints, FL/OD = 11.5e4 (SP1) and 18.5e4 units (SP2), were successfully tracked by the P-controller. However, despite the fast response time of the electronic actuators, both trajectories exhibited noticeable overshoot before gradually converging to their respective setpoints.

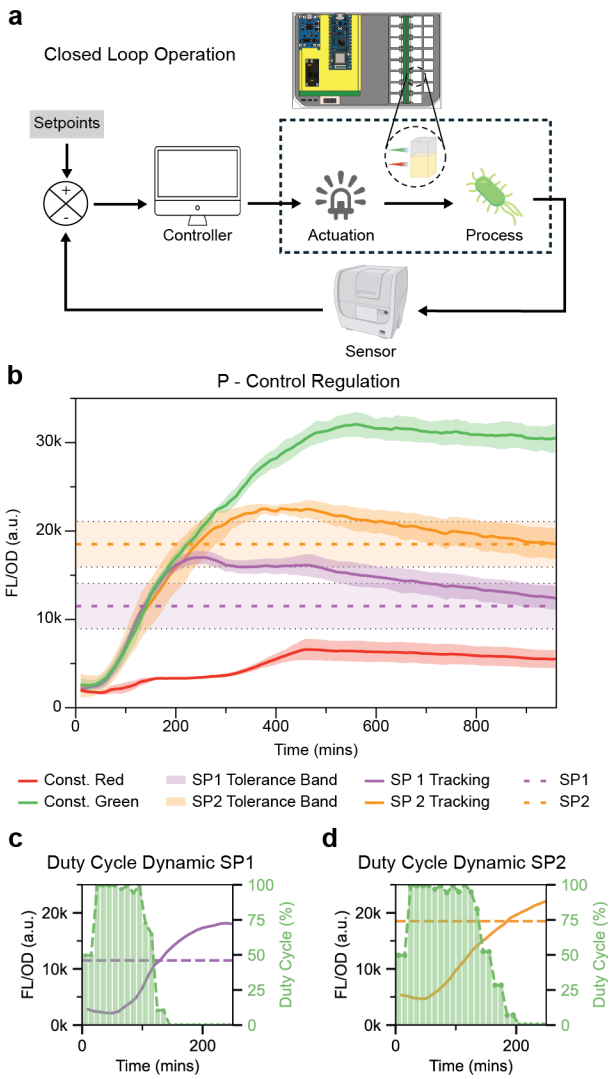


***Figure 3 Closed-loop control in LEMOS*** a) Schematic of closed-loop operation: the microplate reader functions as the sensor that measures FL/OD, the computer functions as the controller, and the LEMOS device actuates LEDs to regulate gene expression. The process plant is gene expression in living bacterial cells. (b) Proportional (P) control tracking of fluorescence setpoints. Constant-light references are green and red (N=4, n=2). Setpoint runs over 2 independent days (N=9, n=2, total 18 trajectories). Solid lines indicate the mean FL/OD; shaded bands indicate standard deviations. Dotted lines mark setpoints (SP1 = $1.15\times10^5$ a.u., SP2 = $1.85\times10^5$ a.u.); shading around setpoints indicate ±10% tolerance. (c–d) Duty-cycle command for representative SP1 and SP2 runs; each panel shows a single well trajectory. N denotes the number of technical replicates; n denotes for the number of biological replicates.

### *Growth-Dependent Dead Time Leads to Signal Overshoot*

To investigate the consistent overshoot observed under P-control regulation, we developed a deterministic kinetic model to capture the system's dynamic behavior. Specifically, we used a Chemical Reaction Network (CRN) to represent the signal sensing and transduction dynamics of the two-component optogenetic system, and a set of ordinary differential equations (ODEs) to model the downstream gene expression process.

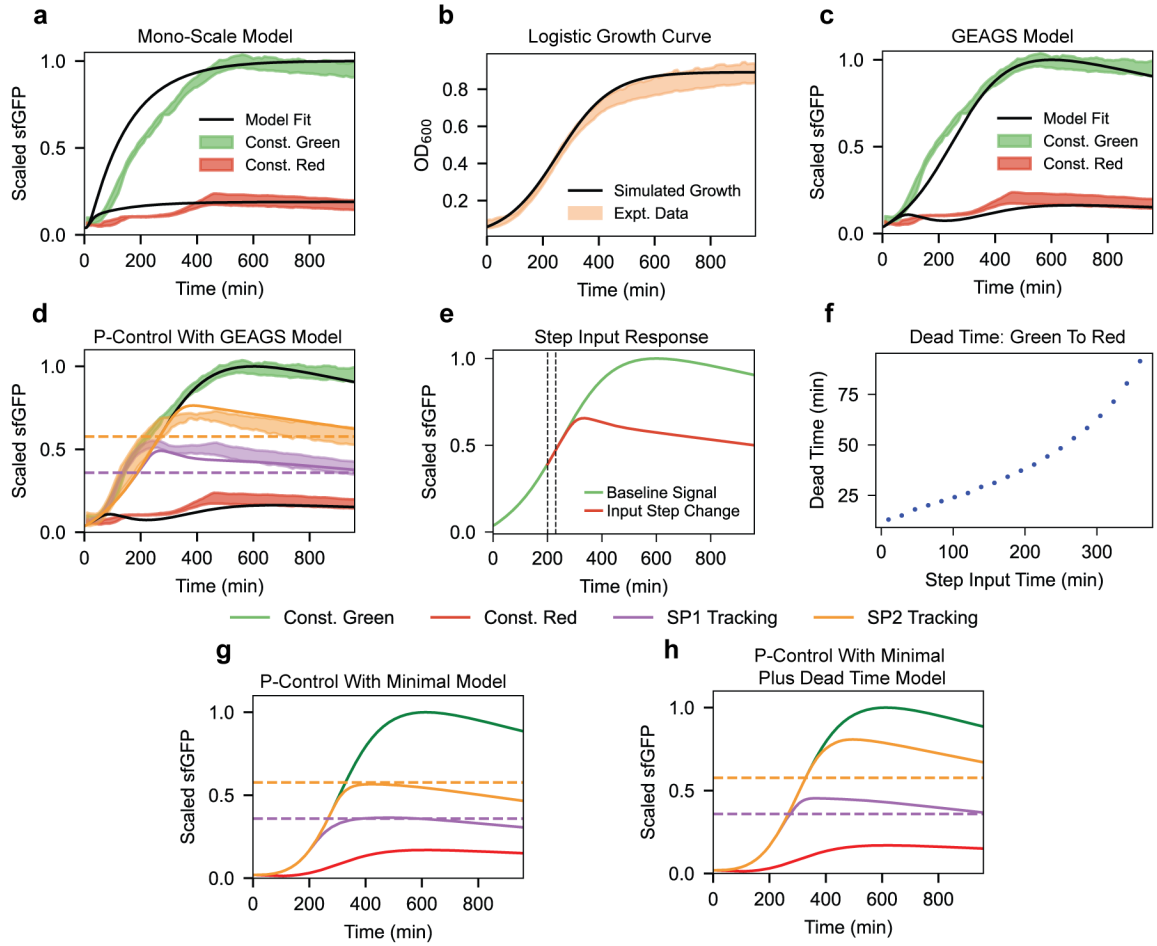


***Figure 4. GEAGS growth-aware modeling explains dead time and P-control behavior.*** a) Single-scale model simulation of scaled sfGFP under constant green light activation and constant red light repression, overlaid with experimental data (N=4, n=2); black solid line indicates the model fit. (b) Simulated logistic growth overlaid with measured $OD_{600}$ (N=18, n=2). (c) Dual-scale GEAGS (Gene Expression Across Growth Stages) model simulation overlaid with the same constant-input data in (a). (d) P-control simulations with the GEAGS model overlaid on experimental setpoint-tracking data. Solid lines indicate model simulation, shaded regions indicate experimental data (N=9, n=2 for set point tracking). Dashed colored lines represent the predetermined setpoint. (e) Step-response simulation with GEAGS model showing dead time when switching the actuator light from green to red at t=200 min (baseline vs. input step change). (f) Response dead time of green-to-red switch increases over time. (g) P-control dynamics simulated with a minimal model omits gene expression dynamics associated time delay (SI section 5), showing minimal system overshoot. (h) P-control dynamics simulated with the same minimal model in (g) with artificial addition of deadtime in (f), recapitulates the observed overshoot. N denotes the number of technical replicates; n denotes for the number of biological replicates.

The kinetics of the sensing component is described with the following CRNs:

$$CcaS \underset{k_{rvrs}}{\overset{k_{fwd}}{\rightleftharpoons}} CcaS_P \tag{2}$$

$$CcaS_P + CcaR \rightleftarrows CcaS + CcaR_P \tag{3}$$

$$CcaR_p + CcaR_p \rightleftarrows Ac \tag{4}$$

$$k_{fwd} = k_{green} + k_{fb} \tag{5}$$

$$k_{rvrs} = k_{red} + k_{rb} \tag{6}$$

These reactions are shown in the schematic Figure 2a. The sensing component of the optogenetic system begins with the transmembrane sensor $CcaS$, which becomes phosphorylated ($CcaS_P$) when exposed to green light. $CcaS_P$ then transfers the phosphate group to the response regulator $CcaR$, producing phosphorylated $CcaR$ ($CcaR_p$), which dimerizes to form the active transcription factor complex $Ac$. This activating complex initiates transcription of the sfGFP gene. To model light-dependent phosphorylation of CcaS, we defined the forward rate constant in equation (2) as the sum of a small basal phosphorylation rate ($k_{fb}$) and the green-light–dependent rate ($k_{green}$) (equation (5)). Under green light, phosphorylation occurs at the full rate $k_{green} + k_{fb}$, whereas in its absence (red light or darkness), only the basal rate applies ($k_{fb}$). Similarly, the $CcaR_p$dephosphorylation rate constant was defined as the sum of a basal dephosphorylation rate $k_{rb}$ and the red-light–dependent rate ($k_{red}$), as described in equation (6). Under red light, dephosphorylation occurs at the full rate $k_{red} + k_{rb}$, while in its absence (green light or darkness), only the basal rate ($k_{rb}$) is applied. The downstream processes of transcription, translation, and protein maturation are captured by the following system of ODEs:

$$\frac{dM}{dt} = \beta \cdot \left(\frac{Ac}{Kc + Ac} + l_0\right) - d_m \tag{7}$$

$$\frac{dP}{dt} = k_{tl} \cdot M - \left(d_p + k_{fold}\right) \cdot P \tag{8}$$

$$\frac{dP_m}{dt} = k_{fold} \cdot P - d_p \cdot P_m \tag{9}$$

Here, $Kc$ is the dissociation constant for the activating complex $Ac$ activating the $P_{cpcG2}$ promoter. The gene expression dynamics were modeled using the standard gene expression modeling framework[31], containing three main species including mRNA ($M$), unfolded sfGFP ($P$), and folded sfGFP ($P_m$). In this system, $\beta$ and $k_{tl}$ represent the transcription and translation rates, respectively; $d_m$ denotes the mRNA degradation rate; $d_p$ accounts for the protein dilution; and $k_{fold}$ represents the protein folding rate.

As shown in Figure 4a, the model simulates sfGFP dynamics under constant red and green light exposure with some discrepancy. Noticeably, it consistently overestimates the initial rate of signal increase when in data fitting. We hypothesize that this discrepancy arises from a key simplifying assumption: all gene expression-related rates in equations (7–9) are treated as constants. This assumption implicitly assumes that cells remain in a state of continuous exponential growth throughout the experiment. In reality, the cells were grown in closed PDMS microwells, forming a batch culture environment. In such conditions, cell growth follows a logistic curve with three phases: lag, exponential, and stationary (Figure 4b). These growth phase transitions affect cellular resources and machinery availability, thereby influencing gene expression rates over time. This introduces multiscale dynamics that a single-scale model with constant parameters cannot fully capture.

To incorporate both growth and gene expression dynamics, we applied our previously established dual-scale Gene Expression Across Growth Stages (GEAGS) model framework[32]. In this model, equations (10-12) replace the earlier gene expression equations (7–9), while the phosphorylation reactions equations (2–4) remain unchanged. The dual-scale model combines ordinary differential equations (ODEs equations (10–12)) and chemical reaction network (CRN equations (14–15)) to capture gene expression dynamics (see SI section 4), with an additional growth equation (equation (13)) representing cell population dynamics.

$$\frac{dM}{dt} = \beta \cdot \gamma \cdot \left(\frac{Ac}{Kc + Ac} + l_0\right) - (d_m \cdot M + d_{dil} \cdot M) - k_{tli_b} \cdot R_{free} \cdot M + k_{tli_u} \cdot C_{TIC} \quad (10)$$

$$\frac{dP}{dt} = k_{tl} \cdot C_{TIC} - \left(d_p \cdot \delta + k_{fold} \cdot \gamma + d_{dil} \cdot \alpha\right) \cdot P \quad (11)$$

$$\frac{dP_m}{dt} = k_{fold} \cdot \gamma \cdot P - (d_p \cdot \delta + d_{dil} \cdot \alpha) \cdot P_m \quad (12)$$

$$\frac{dC}{dt} = k_{gr} \cdot C \cdot \left(1 - \frac{C}{C_{max}}\right) \quad (13)$$

In the growth dynamics equation (13), $C$ represents the cell count and $C_{max}$ is the carrying capacity, defined by the nutrient availability and volume of the batch culture. The rate modifying functions (RMFs), $\alpha$, $\delta$ and $\gamma$, capture how gene expression dynamics change as cells transition through different stages of growth. These RMFs are defined in terms of the normalized cell density $f = \frac{C}{C_{max}}$, which reflects the proximity of the population to its carrying capacity $C_{max}$. The first RMF, $\alpha = 1 - f$, represents the effective rate of cell division as biomass accumulates in the batch culture. In the model, $\alpha$ modulates the dilution rates of mRNA as well as both folded and unfolded sfGFP. The 2nd RMF, $\delta = \frac{f^n}{1+f^n}$, where $n$ is the Hill coefficient, influences the steepness of the function $\delta$. In the model, $\delta$ modulates the degradation of both folded and unfolded sfGFP, capturing the upregulation of proteolysis as cells enter stationary phase. The 3rd RMF $\gamma = \left(f \cdot (1 - f)\right)^m$, reflects the molecular process efficiency across growth phases, peaking during mid-log when growth is most rapid. In the model, $\gamma$ modulates the effective transcription rate, sfGFP folding rate and the coarse-grained translation resource ($R$) availability. Additional parameters in the growth dependent model include $d_{dil}$, the dilution rate due to cell growth, and $k_{tli_b}$ and $k_{tli_u}$, the binding and unbinding rates of the coarse-grained translation initiation complex $C_{tic}$, respectively. The dynamics of $R$ and $C_{tic}$ are captured by the following equations:

$$R_{free} + M \underset{k_{tli_u}}{\overset{k_{tli_b}}{\rightleftharpoons}} C_{TIC} \quad (14)$$

$$C_{TIC} \xrightarrow{k_{tl}} P + M + R_{free} \quad (15)$$

$$R_{total} = R_{max} \cdot \gamma \quad (16)$$

$$R_{free} = R_{total} - C_{TIC} \quad (17)$$

The parameters and the estimated values are described in detail in SI section 4.4. With these modifications, the optogenetic GEAGS model simulation showed strong agreement with experimental data, accurately reproducing sfGFP dynamics under both constant green- and red-light inputs (Figure 4c).

To investigate the consistent overshoot observed in the P-control regulation experiment, we simulated the system using the GEAGS model framework[32]. The simulation results closely matched the experimental data (Figure 4d), capturing the overshoot behavior. This agreement suggests that the overshoot arises from well-understood mechanisms intrinsic to the system. We hypothesize that it is primarily driven by inherent delays in the gene expression process, such as transcriptional and translational lag.

To quantify the system delays, we examined dead time in the optogenetic controlled system. Dead time is defined as the period during which a change in the input has no observable effect on the system output. In this case, the delay between an LED light shifts and the corresponding change in the measured FL/OD signal. To estimate this delay, we first simulated the system under constant green light to establish a baseline FL/OD trajectory (Figure 4e, green curve). We then introduced step changes from green to red light at various time points and measured how long it took for the FL/OD signal to diverge from the baseline. Dead time at each time point t was defined as the duration required to observe a 0.1% change from the baseline FL/OD value (Figure 4e). Because gene expression kinetics are growth-dependent, the system's dead time is not constant over the course of the experiment. As shown in Figure 4f, dead time increases over time, indicating a gradual decline in system responsiveness as the batch culture approaches the stationary phase. This trend is consistent with the general understanding that gene expression slows down as cellular resources are depleted during growth arrest, resulting in increasingly sluggish system dynamics.

To isolate the effect of dead time on closed-loop control dynamics, we first simulated the system using a minimal model that assumes zero delay in gene expression. This model omits delays associated with protein folding and switching of the two-component system (see equations (S25-27), SI Section 5). As expected, the closed-loop simulation with this delay-free model exhibited negligible overshoot (Figure 4g), reflecting the idealized dynamics of the system. To examine the role of deadtime in isolation, we then developed a minimal-plus-dead time model, which extends the minimal model by incorporating experimentally estimated dead time $t_{dt}(t)$, at each time step (outlined in Figure 4f). In this model, sfGFP dynamics were first simulated with P-control. At each time point, $t_i$, the controller calculated the control input (i.e., duty cycle) based on the sfGFP signal at a prior time $t_i - t_{dt}(t_i)$, thereby emulating the effect of system delay. This approach effectively shifts the controller's perception of the current system state, accounting for the time lag introduced by biological processes. The resulting closed-loop simulation with the minimal-plus-dead time model reproduced the overshoot observed experimentally (Figure 4h). These results suggest that the overshoot arises from inherent sluggishness in the biological gene expression process. While the electronic components responsible for sensing, computation, and actuation operate on millisecond timescales, the overall response of the hybrid cell-silicon system is limited by slower biological processes such as transcription, translation, and fluorescent protein maturation.

## *Implementation of PI and PID Feedback Control*

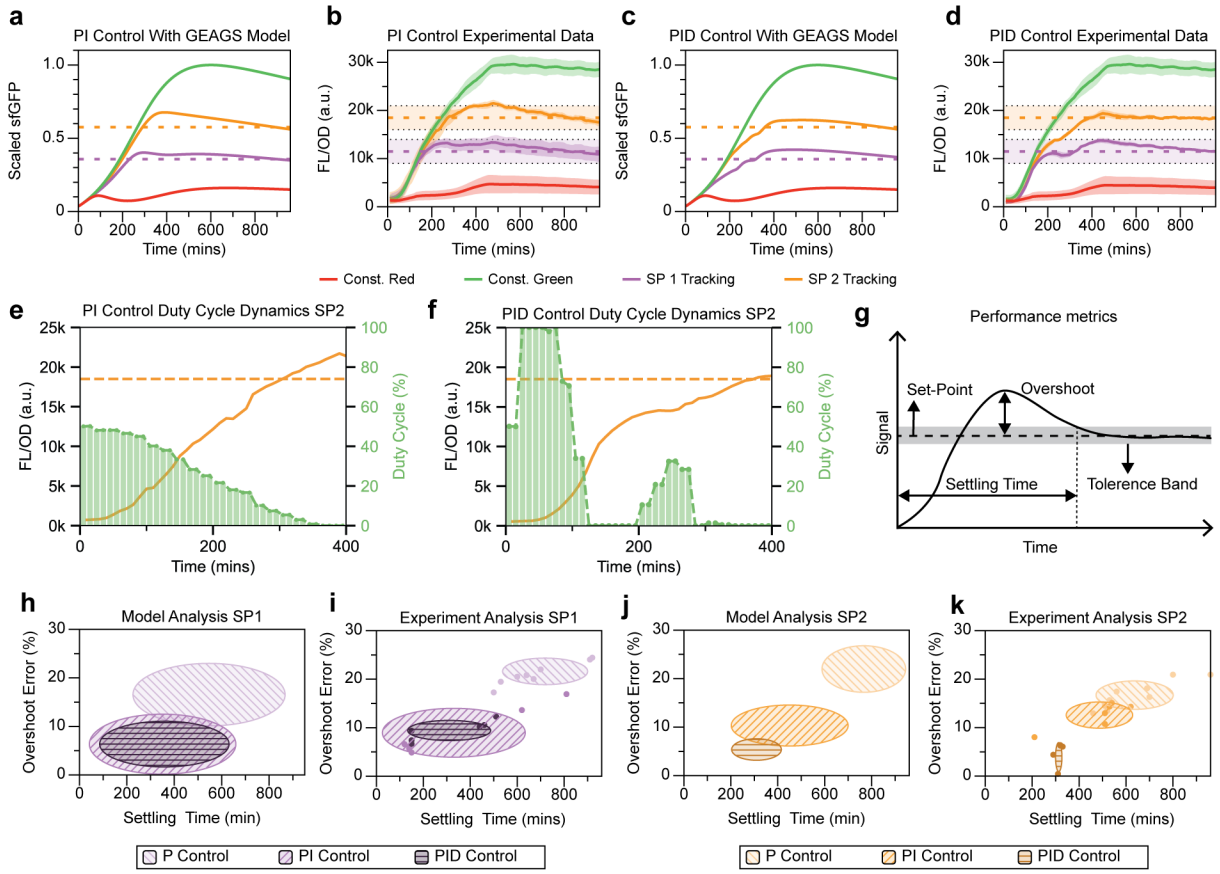


***Figure 5 Model-guided PI and PID regulation.*** (a) GEAGS-based PI control simulations with tuned gains. (b) PI control experiments in LEMOS: constant-light references (N=14, n=6 each) and setpoint tracking at SP1 and SP2 (N=6, n=2 each). (c) GEAGS-based PID control simulations with tuned gains. (d) PID control experiments in LEMOS: constant-light references (N=14, n=6 each) and setpoint tracking at SP1 and SP2 (N=6, n=2 each). (e–f) Duty-cycle command for representative SP2 tracking with PI and PID controller; each panel shows a single well trajectory. (g) Definition of performance metrics: overshoot (%) and settling time to enter and remain within a ±10% band around the setpoint. (h–k) Comparison of P, PI, and PID performance from model predictions (h, j) and experiments (i, k) for SP1 and SP2. N denotes the number of technical replicates; n denotes for the number of biological replicates.

Since the proportional control consistently produced overshoot, primarily due to system dead time and sluggish gene expression dynamics, we next evaluated proportional-integral (PI) and proportional-integral-derivative (PID) controllers. In control theory, PI control eliminates steady-state error by integrating past errors, while PID adds derivative action to improve transient response by anticipating changes in the error[33,34]. These strategies are particularly useful for slow or delay-prone systems, where proportional control alone is insufficient. We implemented both PI and PID schemes to test whether they could achieve more accurate setpoint tracking and faster convergence.

First, we tested whether a proportional-integral (PI) controller could improve controller performance by compensating for accumulated error over time. In PI control, the integral term accounts for the sum of the past errors equation (18), which can and reduce overshoot and improve setpoint tracking accuracy[34]. In our system, the PI controller determined the duty cycle for each

10-minute control period using the following equation:

$$t_{green} = K \cdot \left( e(t) + \frac{1}{\tau_I} \cdot \int e(t)\, dt \right) \tag{18}$$

Here $\tau_I$ is the integral time constant, which scales the accumulated error e(t). Using the GEAGS model, we optimized PI controller gains and selected $\tau_I$ = 1500 min and K = 0.013 min/nM, Simulation showed that the PI controller effectively reduced overshoot and enabled after convergence to both set-points (Figure 5a) compared to P-control dynamics (Figure 3b). We then implemented this model guided design experimentally using the LEMOS plate. The results confirmed consistently low overshoot for both setpoints (Figure 5b), as compared to the P control experiment in Figure 3b. Notably, both simulations and experiments indicated that tracking performance for SP2 was slightly less optimal than for SP1, exhibiting minor overshoot. Based on Figure 5e, we observed that the duty cycle adjustment appears to be insufficiently responsive, contributing to the observed overshoot. This indicates potential for further improvement through controller design.

To further improve setpoint tracking performance, we implemented a proportional-integral-derivative (PID) control strategy. In addition to the proportional and integral terms, PID control includes a derivative term that responds to the rate of change of the error:

$$t_{green} = K \cdot \left( e(t) + \frac{1}{\tau_I} \cdot \int e(t)\, dt + \tau_D \cdot \frac{de(t)}{dt} \right) \tag{19}$$

Here $\tau_D$ is the derivative time constant, which determines how much the slope of the error contributes to the control signal. Derivative action predicts future behavior of the error based on its current rate of change[34]. Using the GEAGS model, we optimized the PID controller parameters and selected $\tau_I = 1500$ min, K = 0.032 min/nM, and $\tau_D = 120$ min. Simulation showed that the PID controller (Figure 5c) significantly reduced overshoot and improved convergence for SP2 compared to PI-control. However, for SP1, the improvement was minimal. Similarly, we experimentally implemented this controller using the LEMOS device. The experimental results aligned with the simulations: PID control enhanced tracking performance for SP2 while having limited additional benefit for SP1 (Figure 5d). As shown in Figure 5f, the duty cycle dynamics exhibit a stair-step–like profile. The sharp increase in signal prior to ≈100 minutes triggered an aggressive controller response, resulting in near-complete suppression of green light. As the rate of signal increase slowed, the controller abruptly raised the duty cycle between 200 and 270 minutes, followed by another sharp reduction at 300 minutes. This pattern likely stems from the derivative term acting on a sluggish system, producing anticipatory but discretely timed adjustments, which is a well-documented behavior in systems incorporating derivative control[33].

To evaluate the performance of the different control strategies, we established two key metrics, as shown in Figure 5g. The system was activated at t = 0, and 10% tolerance band was applied to both setpoints. First, the overshoot error was defined as the maximum deviation between the sfGFP signal and the set-point. Second, the settling time was defined as the time it required for the signal to re-enter the tolerance band after an overshoot.

We generated a performance analysis graph with the overshoot error on the y-axis and the

settling time on the x-axis. On this map, the optimal control strategy lies closest to the origin, corresponding to both fast response (short settling time) and accurate tracking (low overshoot error). We first analyzed SP1 tracking with all three types of controllers (P, PI, and PID). In the GEAGS model simulation, we generated 50 trajectories by perturbing the parameter values by $\pm 15\%$ of the fitted estimates and recorded the corresponding performance metrics. The results showed a clear improvement in both speed and accuracy when moving from P control to PI control, while PID control provided minimal additional benefit (Figure 5h). This same pattern was also reproduced in the experimental data analysis (Figure 5i). We then applied the same analysis to SP2 tracking in both simulation (Figure 5j) and experiments (Figure 5k). In this case, performance improved consistently from P to PI to PID control.

Overall, these results indicate that derivative action was dispensable for SP1 tracking but became essential for SP2. We attribute this difference to growth-phase effects: SP1 was reached earlier, during logarithmic growth when system dead time was small and responsiveness was high, whereas SP2 was reached later, when the system was more sluggish, making derivative control critical for maintaining responsiveness.

**Discussions**

Our work effectively showcases that LEMOS device makes closed-loop optogenetic control as routine as reading OD and fluorescence in a commercial microplate reader. By embedding LEDs in a microplate and blanking illumination during measurement windows, this platform preserves reader sensitivity and removes transfers between stimulation and readout. In batch *E. coli* cultures, proportional control tracked early setpoints but overshot as growth slowed. A growth-aware GEAGS model explained this behavior as growth-dependent dead time, and guided PI and PID designs that improved accuracy and settling across conditions.

Mechanistically, gene expression in batch culture behaves as a process plant whose effective delay increases as cultures approach stationary phase. Transcriptional and translational latencies, protein maturation, and biomass dilution slow the apparent response relative to the controller's sampling period and setpoint changes. Since responsiveness depends on growth phase, a controller tuned for one setpoint or phase may be suboptimal in another. This highlights the multiscale nature of closed-loop gene regulation, where population dynamics shape molecular kinetics and determine which control structures and gains provide robust performance.

The LEMOS device makes closed-loop optogenetic control practical inside the same microplate reader used for routine OD and fluorescence, lowering the barrier to model-informed DBTL and revealing growth-phase effects that are often hidden in chemostats or single-cell rigs. Open-loop kinetics collected with LEMOS guided development of a growth-dependent deterministic model that accurately captures the hybrid system's dynamics and guides controller design. To our best knowledge, this is the first end-to-end DBTL cycle to achieve functional closed-loop optogenetic control in batch culture. Together, the accessible hardware and growth-aware model make DBTL for closed-loop cell-silicon systems a routine workflow, enabling rapid iteration and

more reliable design. Both the device and the modeling framework are generalizable and can be extended to other hosts and optogenetic actuators.

The current LEMOS device offers three illumination channels (red, green, blue; RGB). In this work we used the green and red channels to drive the CCaSR system. The device is ready to evaluate systems using blue-light actuators, such as EL222[35,36], iLID[37], or VVD[38]. Variants can also be built to incorporate different LED lights to test optogenetic systems that are stimulated by, for example, near infrared light[39] and violet light[40]. In addition, we will also use the platform to study layered control in synthetic biology[41] by combining molecular feedback or feedforward circuits with cell-silicon control, and quantify how layering affects setpoint tracking and disturbance rejection performance. On the control-algorithm side, because response speed varies with growth, controller gains should adapt accordingly. We will explore gain scheduling based on OD or online growth-rate estimates, add anti-windup and explicit disturbance-rejection tests, and, leveraging the calibrated GEAGS model[32], implement model predictive control (MPC) that uses short-horizon forecasts to update inputs across phases and setpoints. Together, these extensions will expand LEMOS beyond batch culture and improve robustness across hosts and circuits.

## Methods

### *LEMOS Device and PDMS Microwell Fabrication*

The LEMOS device integrates the electronic components necessary for optical stimulation and wireless communication with an external computer running a Python script. It is built on a 3D-printed PLA frame designed to fit within a standard single-well plate and currently supports 16 microwells with independently controlled LEDs. A full list of components is provided in the SI Section 1. The 16 LEDs in the LEMOS device are connected via a single $I^2C$ bus controlled by an Arduino Nano33 IoT microcontroller, which also includes a Bluetooth module for wireless communication with an external computer. Both the microcontroller and LEDs are powered by an onboard Li-ion battery. Each LED is individually addressable over the $I^2C$ bus, with user-defined control over color and intensity. The emitted wavelengths are determined by the number and type of discrete diodes in each multi-color LED. In this design, we selected commercial LEDs containing three diodes with emission peaks at 620–625 nm, 522–525 nm, and 465–467 nm. Compatible with the regulating spectra (535 nm and 650 nm) of the CcaSR system. These LEDs use pulse-width modulation (PWM) for intensity control, which limits analog tuning. As a result, a fixed intensity was chosen to balance sufficient optical stimulation with minimal heat generation.

PDMS microwells were fabricated in the LEMOS device using standard soft lithography techniques. A 1:10 ratio of the curing and base agents of RTV 615 (Momentive Inc.) was mixed thoroughly and degassed under vacuum in a desiccator for up to one hour to remove air bubbles. It is critical to remove the air bubbles from the PDMS before casting since the bubbles change the optical transmission properties of the bottoms of each well leading to non-uniform baseline OD measurement across wells. The degassed PDMS mixture was then poured into the LEMOS device, into which a 3D-printed PLA mold was inserted to define the shape of the wells. The PDMS in the device was cured overnight at room temperature, after which the PLA mold was carefully removed.

After each experiment the culture in the PDMS microwells were discarded along with the PDMS to reuse the LEMOS device and fabricate new PDMS microwells.

***Experimental Software Programming***

LEMOS operation requires data readout from the microplate reader after each control period (ten minutes), as described in Section 1. On a computer running Biotek Gen5 (the software interfacing the Biotek microplate reader), a custom Python script monitors and collects the exported data after each cycle, storing fluorescence (FL) and $OD_{600}$ values in separate CSV files. If the CSV files do not exist, the script creates them automatically. To avoid export errors from the microplate reader, the script deletes each exported file after processing. In addition to data handling, the script also ensures the microplate reader remains active by issuing appropriate commands, and it performs the necessary calculations for closed-loop control (see GitHub for implementation details).

***Strains and Culture***

The experimental strain was constructed by transforming *E. coli* MG1655 with plasmid pNO286-3 (Addgene #107746) and plasmid pSR58.6 (Addgene #63176). As a negative control for autofluorescence, we constructed an empty backbone by deleting the functional gene cassettes, including $P_{cpcG}2$ and sfGFP, using standard inverse PCR. Cells were plated on LB agar containing 50 μg/mL spectinomycin and 25 μg/mL chloramphenicol and incubated overnight at 37 °C, after which the plates were stored at 4 °C in the dark to minimize light exposure. All experiments were performed in Minimal M9CA Broth (Teknova #M8010) supplemented with 50 μg/mL spectinomycin and 25 μg/mL chloramphenicol. For each condition, a single colony was inoculated into 2 mL of media in a sterile culture tube and grown overnight at 37 °C with shaking at 220 rpm. To prevent unintended light exposure, all cultures were maintained in foil-wrapped tubes. A 100 μL aliquot of the overnight culture was transferred into 2 mL of fresh media in a sterile culture tube and incubated for 4 hours at 37 °C with shaking at 220 rpm. By the end of this period, cultures reached an optical density ($OD_{600}$) of 0.4–0.6. Experimental cultures were then prepared by diluting the pre-culture to an $OD_{600}$ of 0.1, and 200 μL of each condition was added to the PDMS sleeves of the LEMOS device. The device was sealed with a Breath-Easy film (USA Scientific #9123-6100) and loaded into the microplate reader to initiate the experiment. Fluorescence (excitation: 485 nm; emission: 528 nm; gain: 50) and optical density ($OD_{600}$) were measured every 10 minutes using a BioTek Synergy H1 microplate reader, incubated at 30 °C with maximum linear shaking.

***Statistics & Reproducibility***

All single colonies were picked randomly from agar plates where the cells were transformed with purified circular DNA using antibiotics as selection markers. No manual group allocation methods were used. Each plate resulted from an independent transformation, and all colo-

nies were assumed to be biological replicates. No data was excluded from the analyses in experiments presented in Fig. 1e, 1f, 2b, 2c, 2e, 3b, 3c, 3d, 5b, 5d, 5e, 5f, 5i and 5k.

**Acknowledgements:** The authors would like to thank Richard M. Murray for their insightful discussions. This research is partially supported by the Institute for Collaborative Biotechnologies (ICB) through contract W911NF-19-D-0001 from the U.S. Army Research Office. In addition, the author K.P. was also supported by the Caltech Summer Undergraduate Research Fellowships (SURF) program and the Goldwater Foundation. The Authors H.R.N. and B.J. were supported by Texas A&M Engineering Experiment Station.

**Author Contribution:** K.P., C.Y.H., and A.E. conceptualized the project; K.P. designed and built the LEMOS device and wrote the software for LEMOS-PC interface. H.R.N. and C.Y.H. built the ODE models and designed the controllers; B.J., H.R.N., K.P., and C.Y.H. performed the experiments; H.R.N. and B.J performed data analysis; C.Y.H., H.R.N., B.J., and K.P. wrote the manuscript.

**Data and Materials Availability:** All data needed to evaluate the conclusions in the paper are present in the paper and/or the Supplementary Materials. The source code for all the simulations is available at the following GitHub repository: https://github.com/hariKRN2000/LEMOS-models-and-data

## References


1 Hong, L. Y., Li, H., Yang, H. & Sengupta, K. Fully Integrated Fluorescence Biosensors On-Chip Employing Multi-Functional Nanoplasmonic Optical Structures in CMOS. *Ieee J Solid-St Circ* **52**, 2388-2406 (2017). https://doi.org/10.1109/Jssc.2017.2712612

2 Aghlmand, F., Hu, C. Y., Sharma, S., Pochana, K., Murray, R. M. & Emami, A. A 65-nm CMOS Fluorescence Sensor for Dynamic Monitoring of Living Cells. *Ieee J Solid-St Circ* **58**, 3003-3019 (2023). https://doi.org/10.1109/Jssc.2023.3308853

3 Liu, Q. J., Jimenez, M., Inda, M. E., Riaz, A., Zirtiloglu, T., Chandrakasan, A. P., Lu, T. K., Traverso, G., Nadeau, P. & Yazicigil, R. T. A Threshold-Based Bioluminescence Detector With a CMOS-Integrated Photodiode Array in 65 nm for a Multi-Diagnostic Ingestible Capsule. *Ieee J Solid-St Circ* **58**, 838-851 (2023). https://doi.org/10.1109/Jssc.2022.3197465

4 Kumar, S. & Khammash, M. Platforms for Optogenetic Stimulation and Feedback Control. *Front Bioeng Biotechnol* **10**, 918917 (2022). https://doi.org/10.3389/fbioe.2022.918917

5 Ohlendorf, R., Vidavski, R. R., Eldar, A., Moffat, K. & Moglich, A. From dusk till dawn: one-plasmid systems for light-regulated gene expression. *J Mol Biol* **416**, 534-542 (2012). https://doi.org/10.1016/j.jmb.2012.01.001

6 Schmidl, S. R., Sheth, R. U., Wu, A. & Tabor, J. J. Refactoring and optimization of light-switchable Escherichia coli two-component systems. *ACS Synth Biol* **3**, 820-831 (2014). https://doi.org/10.1021/sb500273n

7 Baumschlager, A., Aoki, S. K. & Khammash, M. Dynamic Blue Light-Inducible T7 RNA Polymerases (Opto-T7RNAPs) for Precise Spatiotemporal Gene Expression Control. *ACS Synth Biol* **6**, 2157-2167 (2017). https://doi.org/10.1021/acssynbio.7b00169

8 Sun, Y., Xu, M., Wang, B., Xia, C., He, Z., Lu, B., Cui, J., Liao, Q., Xu, Q. & Gan, F. A Robust and Orthogonal Far-Red Light Sensor for Gene Expression Control in Escherichia coli. *ACS Synth Biol* **14**, 1687-1700 (2025). https://doi.org/10.1021/acssynbio.5c00044

9 Liu, R., Yang, J., Yao, J., Zhao, Z., He, W., Su, N., Zhang, Z., Zhang, C., Zhang, Z., Cai, H., Zhu, L., Zhao, Y., Quan, S., Chen, X. & Yang, Y. Optogenetic control of RNA function and metabolism using engineered light-switchable RNA-binding proteins. *Nat Biotechnol* **40**, 779-786 (2022). https://doi.org/10.1038/s41587-021-01112-1

10 Ranzani, A. T., Wehrmann, M., Kaiser, J., Juraschitz, M., Weber, A. M., Pietruschka, G., Gerken, U., Mayer, G. & Moglich, A. Light-Dependent Control of Bacterial Expression at the mRNA Level. *ACS Synth Biol* **11**, 3482-3492 (2022). https://doi.org/10.1021/acssynbio.2c00365

11 Ranzani, A. T., Buchholz, K., Blackholm, M., Kopkin, H. & Moglich, A. Induction of bacterial expression at the mRNA level by light. *Nucleic Acids Res* **52**, 10017-10028 (2024). https://doi.org/10.1093/nar/gkae678

12 Ruskowitz, E. R., Munoz-Robles, B. G., Strange, A. C., Butcher, C. H., Kurniawan, S., Filteau, J. R. & DeForest, C. A. Spatiotemporal functional assembly of split protein pairs through a light-activated SpyLigation. *Nat Chem* **15**, 694-704 (2023). https://doi.org/10.1038/s41557-023-01152-x

13 Tague, N., Coriano-Ortiz, C., Sheets, M. B. & Dunlop, M. J. Light-inducible protein degradation in E. coli with the LOVdeg tag. *Elife* **12** (2024). https://doi.org/10.7554/eLife.87303

14 McQuillen, R., Perez, A. J., Yang, X., Bohrer, C. H., Smith, E. L., Chareyre, S., Tsui, H. T., Bruce, K. E., Hla, Y. M., McCausland, J. W., Winkler, M. E., Goley, E. D., Ramamurthi, K. S. & Xiao, J. Light-dependent modulation of protein localization and function in living bacteria cells. *Nat Commun* **15**, 10746 (2024). https://doi.org/10.1038/s41467-024-54974-9

15 Milias-Argeitis, A., Rullan, M., Aoki, S. K., Buchmann, P. & Khammash, M. Automated optogenetic feedback control for precise and robust regulation of gene expression and cell growth. *Nat Commun* **7**, 12546 (2016). https://doi.org/10.1038/ncomms12546

16 Gutierrez Mena, J., Kumar, S. & Khammash, M. Dynamic cybergenetic control of bacterial co-culture composition via optogenetic feedback. *Nat Commun* **13**, 4808 (2022). https://doi.org/10.1038/s41467-022-32392-z

17 Lugagne, J. B., Sosa Carrillo, S., Kirch, M., Kohler, A., Batt, G. & Hersen, P. Balancing a genetic toggle switch by real-time feedback control and periodic forcing. *Nat Commun* **8**, 1671 (2017). https://doi.org/10.1038/s41467-017-01498-0

18 Chait, R., Ruess, J., Bergmiller, T., Tkacik, G. & Guet, C. C. Shaping bacterial population behavior through computer-interfaced control of individual cells. *Nat Commun* **8**, 1535 (2017). https://doi.org/10.1038/s41467-017-01683-1

19 Lugagne, J. B., Blassick, C. M. & Dunlop, M. J. Deep model predictive control of gene expression in thousands of single cells. *Nat Commun* **15**, 2148 (2024). https://doi.org/10.1038/s41467-024-46361-1

20 Steel, H., Habgood, R., Kelly, C. L. & Papachristodoulou, A. In situ characterisation and manipulation of biological systems with Chi.Bio. *PLoS Biol* **18**, e3000794 (2020). https://doi.org/10.1371/journal.pbio.3000794

21 Olson, E. J., Hartsough, L. A., Landry, B. P., Shroff, R. & Tabor, J. J. Characterizing bacterial gene circuit dynamics with optically programmed gene expression signals. *Nat Methods* **11**, 449-455 (2014). https://doi.org/10.1038/nmeth.2884

22 Bugaj, L. J. & Lim, W. A. High-throughput multicolor optogenetics in microwell plates. *Nat Protoc* **14**, 2205-2228 (2019). https://doi.org/10.1038/s41596-019-0178-y

23 Repina, N. A., McClave, T., Johnson, H. J., Bao, X., Kane, R. S. & Schaffer, D. V. Engineered Illumination Devices for Optogenetic Control of Cellular Signaling Dynamics. *Cell Rep* **31**, 107737 (2020). https://doi.org/10.1016/j.celrep.2020.107737

24 Hohener, T. C., Landolt, A. E., Dessauges, C., Hinderling, L., Gagliardi, P. A. & Pertz, O. LITOS: a versatile LED illumination tool for optogenetic stimulation. *Sci Rep* **12**, 13139 (2022). https://doi.org/10.1038/s41598-022-17312-x

25 Vogt, A., Paulat, R., Parthier, D., Just, V., Szczepek, M., Scheerer, P., Xu, Q., Moglich, A., Schmitz, D., Rost, B. R. & Wenger, N. Simultaneous spectral illumination of microplates for high-throughput optogenetics and photobiology. *Biol Chem* **405**, 751-763 (2024). https://doi.org/10.1515/hsz-2023-0205

26 Kumar, S., Anastassov, S., Aoki, S. K., Falkenstein, J., Chang, C. H., Frei, T., Buchmann, P., Argast, P. & Khammash, M. Diya - A universal light illumination platform for multiwell plate cultures. *iScience* **26**, 107862 (2023). https://doi.org/10.1016/j.isci.2023.107862

27 Harmer, Z. P. & McClean, M. N. Lustro: High-Throughput Optogenetic Experiments Enabled by Automation and a Yeast Optogenetic Toolkit. *ACS Synth Biol* **12**, 1943-1951 (2023). https://doi.org/10.1021/acssynbio.3c00215

28 Soffer, G., Perry, J. M. & Shih, S. C. C. Real-Time Optogenetics System for Controlling Gene Expression Using a Model-Based Design. *Anal Chem* **93**, 3181-3188 (2021). https://doi.org/10.1021/acs.analchem.0c04594
29 Benman, W., Datta, S., Gonzalez-Martinez, D., Lee, G., Hooper, J., Qian, G., Leavitt, G., Salloum, L., Ho, G., Mhatre, S., Magaraci, M. S., Patterson, M., Mannickarottu, S. G., Malani, S., Avalos, J. L., Chow, B. Y. & Bugaj, L. J. High-throughput feedback-enabled optogenetic stimulation and spectroscopy in microwell plates. *Commun Biol* **6**, 1192 (2023). https://doi.org/10.1038/s42003-023-05532-4
30 Namboothiri, H. R., Pandey, A. & Hu, C. Y. Resolving Emergent Oscillations in Gene Circuits with a Growth-Coupled Model. *bioRxiv*, 2025.2007. 2009.663992 (2025). https://doi.org/10.1101/2025.07.09.663992
31 Alon, U. *An introduction to systems biology: design principles of biological circuits*. (Chapman and Hall/CRC, 2019).
32 Namboothiri, H. R., Pandey, A. & Hu, C. Y. Resolving Emergent Oscillations in Gene Circuits with a Growth-Coupled Model. *bioRxiv*, 2025.2007.2009.663992 (2025). https://doi.org/10.1101/2025.07.09.663992
33 Kravaris, C. & Kookos, I. K. *Understanding process dynamics and control*. (Cambridge University Press, 2021).
34 Åström, K. J. & Murray, R. *Feedback systems: an introduction for scientists and engineers*. (Princeton university press, 2021).
35 Jayaraman, P., Devarajan, K., Chua, T. K., Zhang, H., Gunawan, E. & Poh, C. L. Blue light-mediated transcriptional activation and repression of gene expression in bacteria. *Nucleic Acids Res* **44**, 6994-7005 (2016). https://doi.org/10.1093/nar/gkw548
36 Motta-Mena, L. B., Reade, A., Mallory, M. J., Glantz, S., Weiner, O. D., Lynch, K. W. & Gardner, K. H. An optogenetic gene expression system with rapid activation and deactivation kinetics. *Nat Chem Biol* **10**, 196-202 (2014). https://doi.org/10.1038/nchembio.1430
37 Guntas, G., Hallett, R. A., Zimmerman, S. P., Williams, T., Yumerefendi, H., Bear, J. E. & Kuhlman, B. Engineering an improved light-induced dimer (iLID) for controlling the localization and activity of signaling proteins. *Proc Natl Acad Sci U S A* **112**, 112-117 (2015). https://doi.org/10.1073/pnas.1417910112
38 Sternberg, J. B. & Pierce, N. A. Exquisite sequence selectivity with small conditional RNAs. *Nano Lett* **14**, 4568-4572 (2014). https://doi.org/10.1021/nl501593r
39 Ong, N. T., Olson, E. J. & Tabor, J. J. Engineering an E. coli Near-Infrared Light Sensor. *ACS Synth Biol* **7**, 240-248 (2018). https://doi.org/10.1021/acssynbio.7b00289
40 Zhang, W., Lohman, A. W., Zhuravlova, Y., Lu, X., Wiens, M. D., Hoi, H., Yaganoglu, S., Mohr, M. A., Kitova, E. N., Klassen, J. S., Pantazis, P., Thompson, R. J. & Campbell, R. E. Optogenetic control with a photocleavable protein, PhoCl. *Nat Methods* **14**, 391-394 (2017). https://doi.org/10.1038/nmeth.4222
41 Hu, C. Y. & Murray, R. M. Layered feedback control overcomes performance trade-off in synthetic biomolecular networks. *Nat Commun* **13**, 5393 (2022). https://doi.org/10.1038/s41467-022-33058-6